Particle Physics at CERN

Annual Report 2003

C. Amsler, V. Chiochia, A. Dorokhov, A. Giacomin, A. Glauser, C. Hörmann,
O. Iannarelli, I. Johnson, K. Prokofiev, H. Pruys, C. Regenfus,
P. Robmann, J. Rochet, T. Speer and S. Steiner

Physik-Institut der Universität Zürich
Winterthurerstrasse 190, CH-8057 Zürich, Switzerland

April 2, 2004

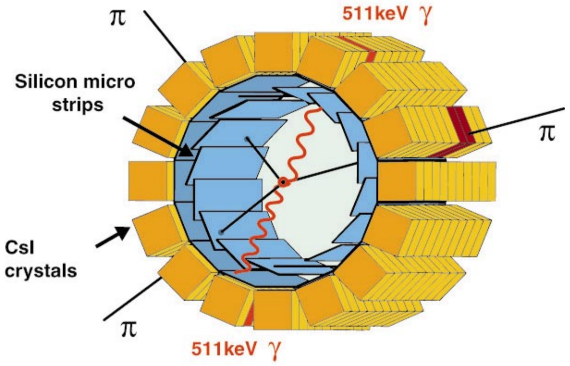

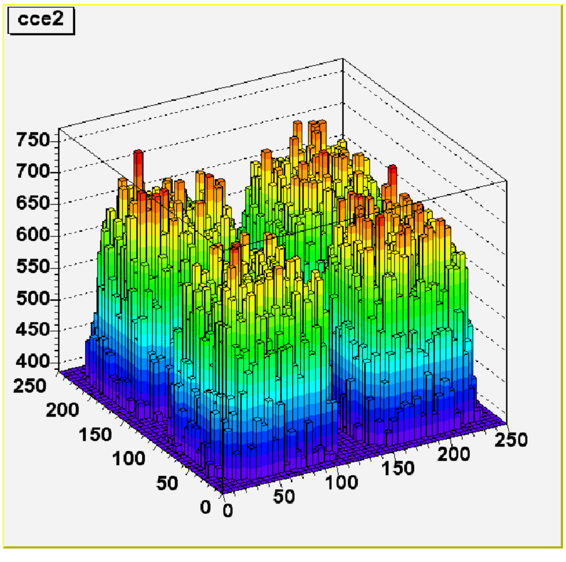

Contents

This report covers the two main activities of our group on the ATHENA and CMS experiments between 1 April 2003 and 31 March 2004. Our involvement in the MUNU experiment (measurement of the magnetic moment of the electron-antineutrino at the Bugey nuclear power plant) was completed in 2002 and led the PhD thesis of Oliver Link. Details can be found in our annual report 2002. Also, the present report does not include the activity of one of us (C.A.) within the Particle Data Group, contributing to the next issue of the “Review of Particle Physics” and the “Particle Physics Booklet” which will appear shortly. Further details on the group activities and publication reprints can be obtained from our home page (http://unizh.web.cern.ch/unizh/doc/zuerich.html).

1 Production and Spectroscopy of Antihydrogen

C. Amsler, A. Giacomin, A. Glauser, O. Iannarelli, I. Johnson, H. Pruys, C. Regenfus, and J. Rochet

In collaboration with: CERN, University of Aarhus, Brescia, Genoa, Pavia, RIKEN,
Rio de Janeiro, Swansea, Tokyo (ATHENA Collaboration).

1.1 Introduction

The first observation of cold antihydrogen ($\bar{H}$) was reported in 2002 by the ATHENA collaboration [1]. This breakthrough has stimulated renewed interest in the field of low energy antimatter, and comparisons of the properties of antimatter with those of matter. For future laser spectroscopy experiments the temperature and quantum state of the $\bar{H}$ atom have to be controlled. In 2003 we therefore concentrated on the mechanism underlying the formation of $\bar{H}$, when low energy antiprotons are merged with a dense and cold positron plasma. We have also begun installing a laser system that allows specific $\bar{H}$ states to be addressed.

Antihydrogen is formed in a nested Penning trap by mixing 10^4 antiprotons with a positron plasma containing up to 10^8 particles at a temperature of 15 K. Low energy antiprotons from the CERN antiproton decelerator (AD) are moderated and captured in a Penning trap and are cooled to the ambient temperature of 15 K (1.3 meV) by a preloaded electron plasma. The capture efficiency is about 0.4 %, mainly determined by energy straggling in the absorber. Antihydrogen begins to form after the overlap of the antiprotons with the positrons, with initial production rates in excess of 300 Hz. The characteristics of the positron plasma such as the number of particles, the dimensions (typically 2 cm in length, 2 mm in width) and the density (10^8-10^9 cm^{-3}) can be obtained with a non-destructive method based on a measurement of the low-order axial electrostatic modes of the plasma [2]. The raw experimental data are the resonant frequencies of the first two modes (dipole and quadrupole), and the equivalent inductance of the plasma. The plasma diagnostic, coupled with radio-frequency heating, can be used to monitor and control changes in the plasma temperature. Antihydrogen formation at 15 K will be called "cold mixing" while positron-antiproton mixing with a positron plasma heated to $\sim$ 3000 K will be referred to as "hot mixing.

The neutral $\bar{H}$'s are not confined by the electric and magnetic fields and therefore migrate to the trap walls where they annihilate. These events are monitored by the $\bar{H}$ detector built by the University of Zurich [3]. The detector consists of two layers of double-sided silicon strip detectors to register the charged annihilation pions and to reconstruct the annihilation vertex. Antihydrogen is detected by requiring the spatial and temporal coincidence of the vertex with two back-to-back 511 keV γ's produced by the annihilation of the positron. The γ's are detected by a high granularity electromagnetic detector comprising 192 CsI crystals with avalanche photodiode readout. A comprehensive description of the ATHENA apparatus can be found in ref. [4].

1.2 Antihydrogen production efficiency

The observation of cold $\bar{H}$ was based on a complete reconstruction of its annihilation, in which both antiprotons and positrons were detected via their annihilation products. We reported 131 ± 22 "golden events" [1]. However, the detection efficiency was low ($\simeq$ 0.2%), mainly due to the 20% detection efficiency for each of the two 511 keV photons, and stringent software cuts. In a further analysis [5] we show that the trigger rate during cold mixing is due to two sources: $\bar{H}$ production itself comprises over 85% of the triggers at the beginning of mixing, and declines with a time constant of several seconds. Antiproton annihilation on positive ions or on rest gas (with a slowly decreasing rate) comprises the remainder of the triggers. During a complete cold mixing cycle $\bar{H}$ production accounts for (65 ± 5)% of the total integrated trigger rate. Thus in 2002 almost 500,000 $\bar{H}$ atoms were produced.

In fig. 1.1 (left) we show the photon energy spectrum for cold mixing and for antiprotons only, normalized to the same number of annihilation vertices. No peak is observed at 511 keV for the annihilation of antiprotons only. These are good news since we feared earlier that the background from positron annihilation from high energy showers in the surrounding coils would be much more severe. The difference plot (fig. 1.1, right) shows the 511 keV line from positron (antihydrogen) annihilation, together with a pure positron (no $\bar{p}$) annihilation spectrum. Peak position and resolution agree.

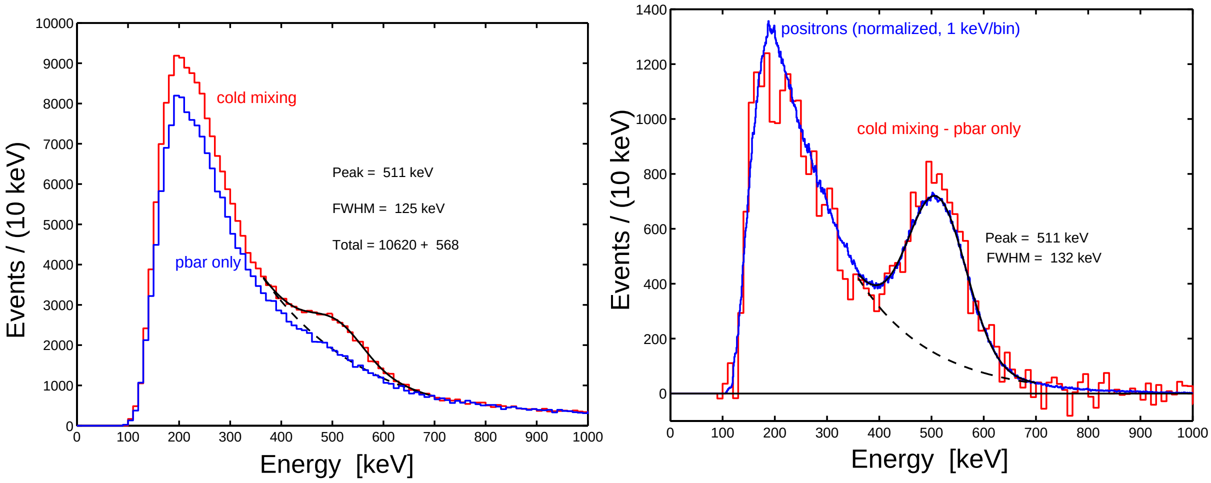

Figure 1.1: *Left: Photon spectrum (sum of the 162 best crystals) for cold mixing and antiprotons only. Right: difference plot and annihilation spectrum from a pure positron plasma superimposed.*

1.2.1 Orthopositronium production

The detection of antihydrogen relies on the reconstruction of two back-to-back 511 keV photons. However, orthopositronium could be produced when positrons annihilate on the trap walls. The contribution from orthopositronium (which decays into 3γ) is unknown since it depends on a possible frozen gas layer on the trap electrode surface at cryogenic temperatures. A large production rate could lead to an underestimate of our antihydrogen formation rate.

A dedicated measurement with positrons only was therefore performed to determine the relative rates of the 2γ and 3γ decay modes of e^+e^- annihilations for antihydrogen atoms interacting with the electrode surfaces [5]. The electrostatic well holding the positrons was modified so that the radial outward transport of positrons onto the trap electrodes was strongly enhanced. The photons produced in positron annihilations at the surface of the electrodes were detected in the photon detector. The trigger condition required the detection of at least two photons with an energy greater than 150 keV each. For events containing two or three photons, the total energy E_{tot} and the total momentum P_{tot} were determined. Figure 1.2a shows the clear signal from 2γ events at E_{tot} = $2m_ec^2$ and $P_{tot} < 200$ keV/c. The accumulation of events at P_{tot} = E_{tot} stems from 2γ events for which one γ escaped detection, while the other underwent Compton scattering in the first crystal before being absorbed by the second adjacent crystal. This process also accounts for most detected 3γ events, stemming from 2γ events, for which one γ is Compton scattered in a first and detected in a second crystal. Figure 1.2b shows a distribution for 3γ events satisfying the condition $|E_{tot} - 2m_ec^2| < 200$ keV. The total momentum of the 3γ is plotted versus the smallest of the three angles between any 2γ. Compton scattered photons accumulate at small angles. The box indicates the expected orthopositronium signal region. The detection probabilities for the two decay modes were evaluated by Monte Carlo simulation. From the observed number of events we could conclude that 2γ events account for at least 95% of all e^+e^- annihilations.

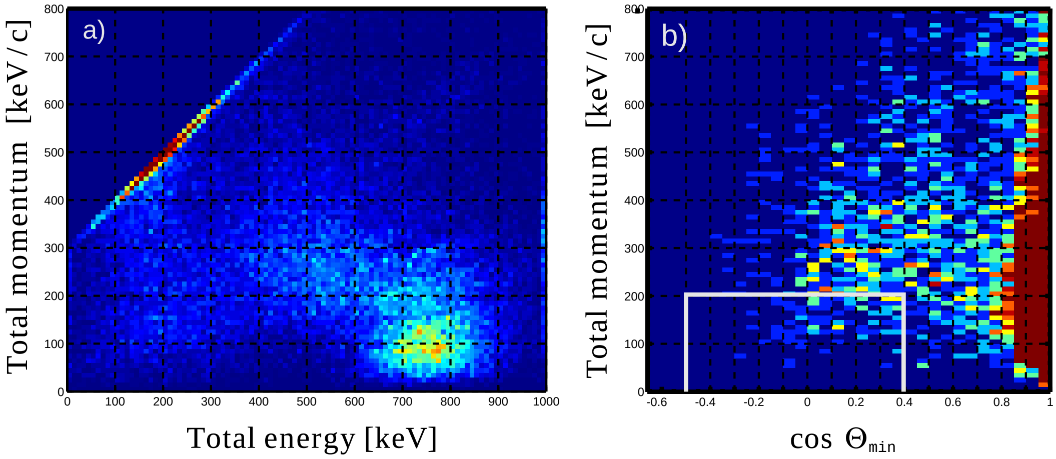

Figure 1.2: *a)* P_{tot} *vs.* E_{tot} *for* 2γ*-events; b)* P_{tot} *vs. minimum* 2γ*-opening angle for* 3γ *events. The box shows the expected region for orthopositronium annihilation.*

1.2.2 Optimization of $\bar{H}$ Rate

Combining hot and cold mixing data we have produced so far in excess of 2 million $\bar{H}$ atoms. However, this corresponds only to about 17% of the antiprotons injected into the trap. Possibilities to increase this formation rate were studied in 2003. For example, positron plasma compression can be achieved using the so-called “rotating wall” method in which the plasma is spun by applying a rotating electric field of several hundred kHz to a segmented trap electrode. The segmented Faraday cup detector in the positron accumulator was replaced with a phosphor screen and an auxiliary low-noise CCD camera. This enables a more accurate measurement of the position and size of the positron plasma (fig. 1.3) before it is transferred to the ATHENA mixing trap located inside the main 3T magnet. We achieved plasma densities of up to 10^{10} e^+ cm^{-3}, which is the highest density positron plasma achieved worldwide to date.

Attempts were also made to increase the number of positrons available for $\bar{H}$ formation by stacking successive shots of positrons from the positron accumulator in the mixing trap. Figure 1.4 shows the number of stacked positrons in the main magnet versus the number of transfers. In this way we were able to reach positron plasmas containing 1.2×10^9 positrons, again the highest number of stored positrons achieved anywhere to date.

Modifications to the ATHENA trap are being carried out to implement the so-called “side band excitation” of the radial $\bar{p}$ motion to reduce the $\bar{p}$ plasma size and increase the overlap with the e^+ cloud: Due to the degrader foil, captured antiprotons have large initial axial, magnetron, and modified-cyclotron amplitudes. While the axial and cyclotron motions are quickly damped through collisions with electrons, the large magnetron radii of the confined antiprotons are retained throughout the entire stacking, transfer, and measurement cycle. This leads to both reduced transfer efficiency and reduced $\bar{H}$ production due to poor radial overlap with the positron plasma. The two independent radial motions carried out by charged particles, the magnetron motion and the modified cyclotron motion, can be resonantly excited by azimuthal radio-frequency electric fields. Quadrupolar excitation at the sum frequency of the two modes (the true cyclotron frequency, 45 MHz in ATHENA) leads to a coupling and energy exchange between them. In the absence of a cooling mechanism, this can

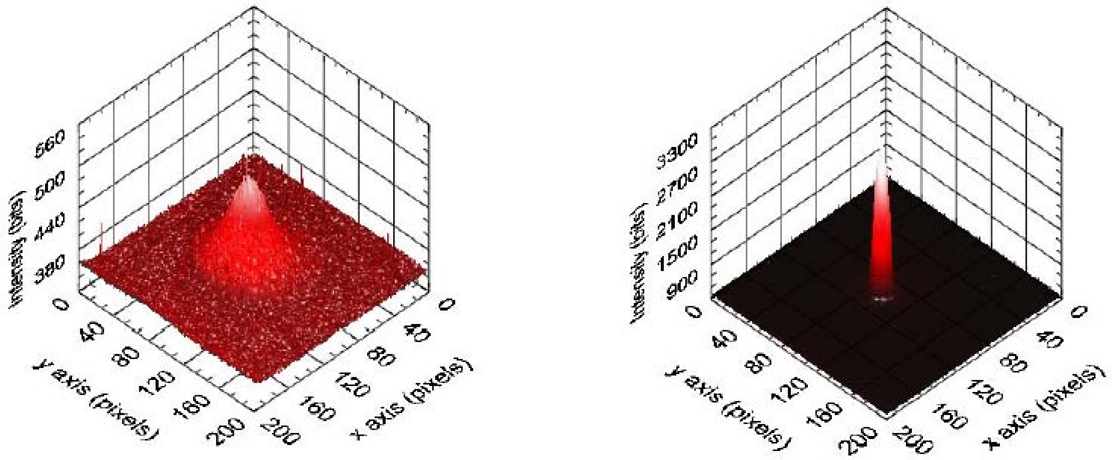

Figure 1.3: *CCD images of the position and size of the positron plasma dumped on the phosphor screen in the positron accumulator without (left) and with (right) rotating wall compression.*

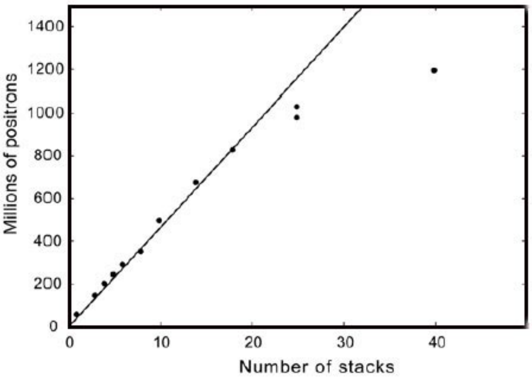

Figure 1.4: *Stacking successive shots of positrons from the positron accumulator. The line is a fit to the data up to 20 stacks and shows the linear behaviour. The fit shows that 50 million positrons per stack were captured.*

be used to transform low-frequency, low-energy magnetron motion into high-frequency, high-energy cyclotron motion. In the presence of a cooling mechanism the modified cyclotron motion would be quickly damped and the total radial motion centered. No significant improvement in the $\bar{H}$ production rate was achieved so far. This issue will be pursued in 2004.

1.3 Dynamics of Antihydrogen Formation

We have measured the antiproton energies during cooling and while $\bar{H}$ is efficiently formed [6]. Figure 1.5a shows the measured antiproton energy spectra at various times during the mixing cycle and fig. 1.5b the W-shaped nested penning trap potential with the positrons in the middle. The antiprotons were ejected from the entrance well and their intensity measured as a function of electric potential. The antiproton potential energy is divided into three regions (labelled I-III in fig. 1.5a). Region I corresponds to $\bar{p}$ energies larger than positron energies, region II to $\bar{p}$'s within the positron space charge, whilst in the lowest energy region III antiprotons no longer have sufficient kinetic energy to penetrate the positron cloud.

The antiprotons ejected from the left well under cold mixing conditions begin to cool rapidly and after about 20 ms a significant fraction ($\simeq$ 40%) reach energies close to the bottom of the positron well. It is here that they are moving slowest as they traverse the positron cloud, and under these

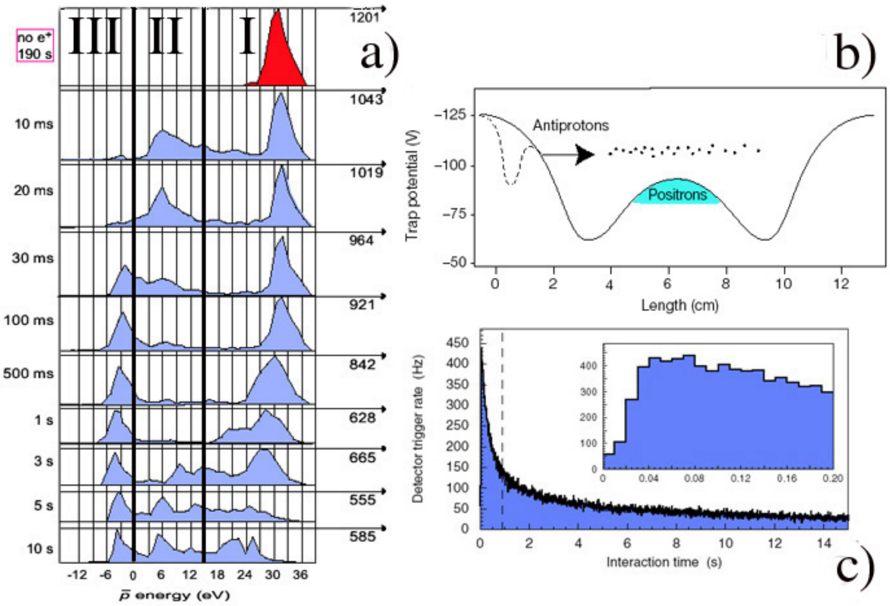

Figure 1.5: *a) Antiproton energy spectra for different interaction times. The interaction time is shown on the left, the maximum peak height in each distribution is indicated on the right. The vertical thick lines divide the three energy regions (see text); b) nested Penning trap potential; c) Trigger rate vs. time for cold mixing. The inset shows an expansion of time between 0 and 0.2 seconds illustrating the onset of $\bar{H}$ production at about 20 ms.*

conditions one might expect $\bar{H}$ to form. This is borne out by the data shown in fig. 1.5c where the $\bar{H}$ detector trigger rate shows a dramatic increase after 20 ms. On longer time scales, though $\bar{H}$ is still copiously formed, there are many antiprotons that retain kinetic energies close to those on injection. This indicates only weak coupling to the positron plasma, possibly due to poor radial overlap. There is also a slow transfer of antiprotons into region III, since antiprotons are present in both the left and right wells at longer times. The precise manner in which the antiprotons cool below the lowest positron energy is not yet clear, but may involve field ionisation of weakly bound $\bar{H}$. A measurement without positrons is included in fig. 1.5a and, as expected, no antiproton cooling is apparent.

We have also measured the temperature dependence of $\bar{H}$ formation [7]. The two processes that lead to $\bar{H}$, radiative combination (in which a photon removes the binding energy) and three-body combination (in which a second positron removes the excess energy), lead to different n-state distributions. The former populates mainly the low n states and the latter mainly the high n states. The $\bar{H}$ production rate has also a different dependence on temperature, $T^{-1/2}$ for the former and $T^{-9/2}$ for the latter.

As explained above, the positron plasma temperature could be changed in a controlled way by radio-frequency excitation. The minimum measurable temperature increase was about 15 meV ($\sim$ 175 K). The electrode temperature of 15 K was the lower limit for the unheated plasma, and this was adopted as the unperturbed temperature. Mixing was carried out at different positron plasma temperatures including the cold mixing data (15 K) and three other high statistics hot mixing samples at 190 K, 515 K and 3500 K. The measurements were analysed in a variety of ways by measuring (a) the 2γ opening angle excess enhancement, (b) the number of triggers for all samples and (c) the peak trigger rates for the high statistics samples. The 2γ opening angle distribution is shown in fig. 1.6 (left). One observes from the enhancement at low $\cos\Theta_{\gamma\gamma}$ that $\bar{H}$ production decreases with temperature, but is still produced at room temperature. This favours radiative over three-body combination.

The temperature dependence of $\bar{H}$ is shown for the three methods in fig. 1.6 (right). One observes a clear decrease of the $\bar{H}$ production with positron plasma temperature. However, a simple power law does not fit the data. The three-body temperature dependence ($T^{-9/2}$) is not consistent with data. Again this favours radiative over three-body recombination. However, the radiative rate prediction is not obviously compatible with our data, being an order of magnitude lower. More work is necessary to definitively clarify the underlying mechanism.

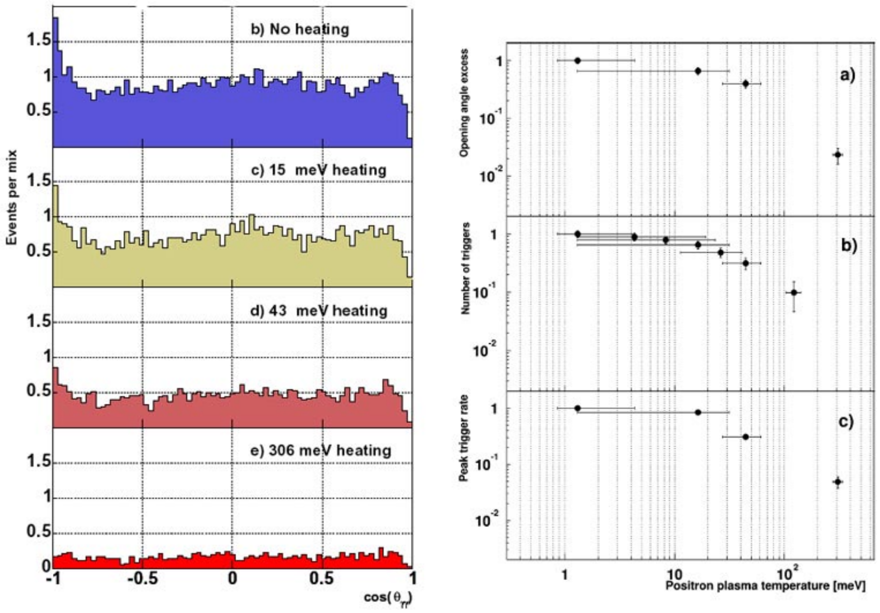

Figure 1.6: *Left: cosine of the opening angle distribution for different positron plasma temperatures* $\sim$ *15 K, 190 K, 515 K and 3500 K (top to bottom, normalized to the mixing of 10'000* $\bar{p}$ *with 7*$\times$ 10^7 e^+*). The peak at -1 is due to* e^+e^- *annihilation of* $\bar{H}$ *atoms hitting the electrodes. Right: temperature dependence of* $\bar{H}$ *production (a) for the opening angle excess, (b) the number of triggers, and (c) the peak trigger rates. Data are normalised to the 15 K sample.*

We also measured the spatial distribution of the emerging $\bar{H}$ atoms which can also provide insights into dynamics of the formation process and the distribution of initial atomic states. Figure 1.7 shows the measured distribution compared to a set of model distributions. The model that best matches the measurements is a slightly anisotropic distribution with a small radial excess. The near-isotropic nature of the distribution suggests that $\bar{H}$ is mostly formed when the antiprotons are diffusing randomly in the positron plasma. Calculations suggest that weakly bound states (populated mostly by the three-body mechanism) would emerge along the lines of the magnetic field. Therefore, the observed isotropic emergence suggests that three-body combination may not be the dominant $\bar{H}$ formation mechanism in ATHENA, in accord with the temperature measurements discussed above.

1.4 Mesurements and improvements on detector performances

Improvements to the detector readout were made to enhance the sensitivity and extend the capabilities of the ATHENA apparatus. The 32 Si μstrip modules of the detector are now read out in a zero suppressed mode so that the detector can be read out at a much higher rate of 200 Hz. One consequence is a substantial increase in baseline fluctuations in the raw crystal data. At readout rates near 200 Hz electronic baselines of the crystals can fluctuate by more than 5 times the average noise. The readout chips are the cause of these fluctuations, since each row of 12 crystals is read out by one readout chip and baselines of crystals within each row move together. Figure 1.8 illustrates the row-by-row

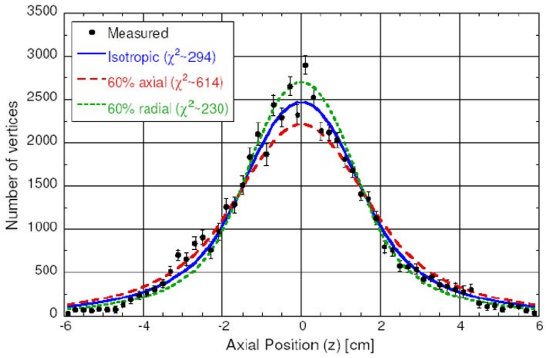

Figure 1.7: *Comparison between isotropic, axially and radially enhanced axial vertex distributions of $\bar{H}$ annihilations. A typical plasma length of 32 mm was used. The data are almost compatible with isotropic emission (blue curve).*

correlation of the baseline fluctuations. New row-by-row baselines for each event are calculated by averaging the ADC values of the groups of 12 crystals (ignoring of course crystals with signals). The new row-by-row baselines are subtracted from the data to obtain ADC distributions that oscillate around zero, see fig. 1.8.

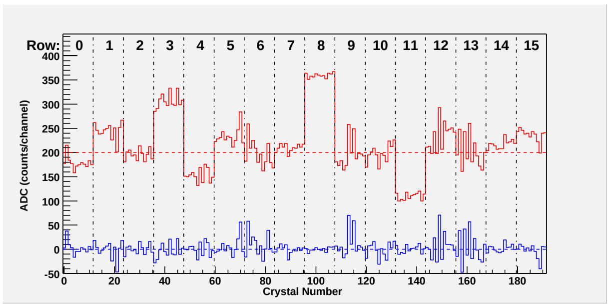

Figure 1.8: *ADC versus crystal channel distributions for a typical readout rate near 200 Hz. Upper distribution: before common-mode-noise correction (artificially offset from 0 by 200 ADC counts). Note the common offsets for rows of 12 crystals connected to the same amplifier chip. Lower distribution: after a row-by-row common-mode-noise correction.*

1.4.1 Measurement of the Lorentz angle

In the presence of the 3 T field the charge carriers (the holes in our detector) do not migrate radially along the electric field but are deflected by the Lorentz angle. Hence the cluster size of the collected charge is modified and its centroid displaced on the readout side. Under the drift along the Lorentz angle λ, the cluster lengths L_c is shortened for tracks that traverse the silicon at angles in the direction of the Lorentz deflection, and increased for tracks that cross in the opposite direction (fig. 1.9).

Our sensors are orientated around two cylinders. The propagation direction of the holes is inward for the inner layer and outward in the outer layer. This results in opposite Lorentz angle displacements that can substantially modify the helix parameterization of the tracks and deteriorate the determination of the annihilation vertex.

We therefore measured the Lorentz deflection angle λ at 130 K. Measurements were made with cosmic rays with field off and on. Figure 1.9b shows for example the average cluster size (number of adjacent hit strips) for tracks in the plane perpendicular to the detector axis ($\phi \simeq 0$) and traversing the silicon layer under the angle θ. The symmetry about θ = 0 in the field off data indicates that charge is propagating along the electric field perpendicular to the plane of the silicon, as expected, while the asymmetry in the distribution of the 3 T data clearly indicates that the holes propagate along a non-zero Lorentz angle.

Since the cluster size also depends on the total charge deposited and hence on the track inclination ϕ along the detector axis, the data were subdivided in ϕ intervals and fits were performed for each bin to determine λ. The strip pitch (139.5 μm) and detector thickness (380 μm) were fixed to their

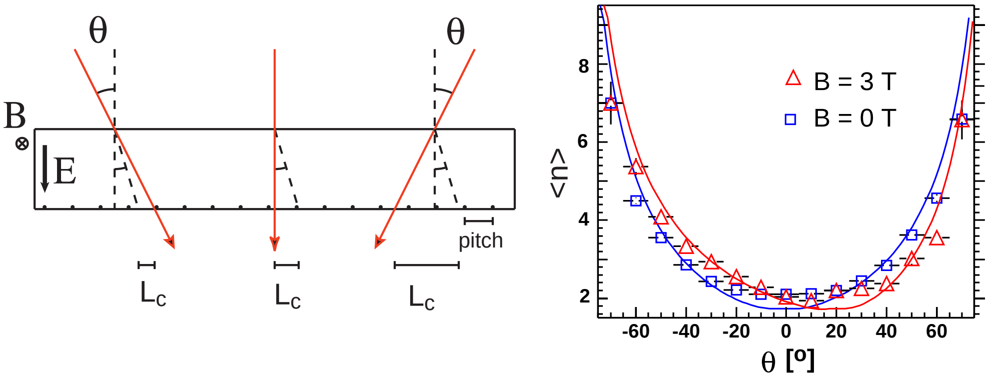

Figure 1.9: *Left: the Lorentz angle λ leads to different cluster lengths L_c that depend on the incident angle θ. Right: cluster size distribution for tracks in the plane perpendicular to the detector axis as a function of θ.*

known values, while the charge detection threshold was left as a free parameter. The results shown in fig. 1.10a do not depend on ϕ, as expected. We obtain a Lorentz angle λ = (18.8 ± 0.5) ° for holes at 130 K and 3 T, while for the field off data λ was consistent with zero.

In order to correct for the displacement caused by the drift along the Lorentz angle, all cluster positions were then shifted by -64.5 μm in the $\vec{E} \times \vec{B}$ direction. This led to a significant improvement in the residuals for traversing cosmic rays which are now in good agreement with the unaffected field off distributions (fig. 1.10b).

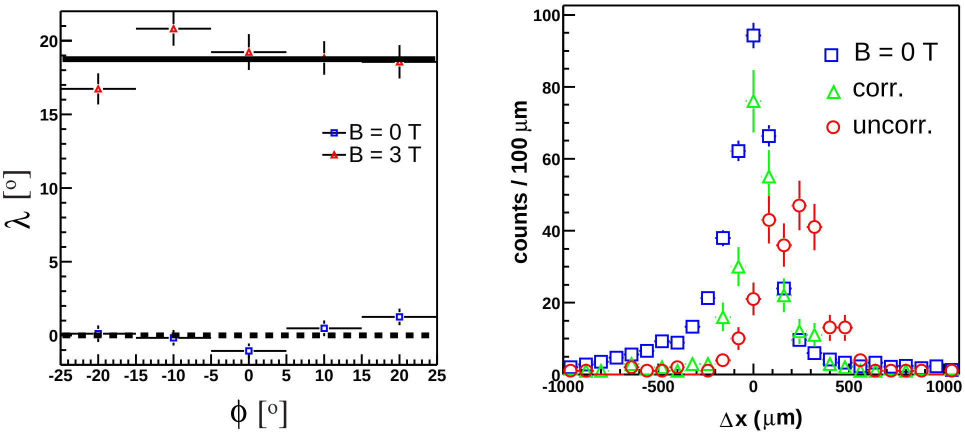

Figure 1.10: *Left: distribution of the Lorentz angle λ vs. ϕ (track angle along the detector axis) for field on and off. Right: shift in the reconstructed position of traversing cosmic rays for field on (red) and off (blue). The shifts after correction are shown in green.*

1.4.2 R & D on CsI crystals

Pure CsI was chosen in ATHENA because of the excellent light yield at low temperature [8]). Initially, the crystals were coupled to pn photodiodes, but their performances deteriorated with time, due to corrosion from the iodine of CsI. We therefore replaced them with avalanche photodiodes (APD) which have gains and hence much better signal-over-noise ratios. A systematic study of the response of SINTEF and avalanche photodiodes as a function of temperature and wavelength was performed with an optical spectrometer based on an Echelette grating [9].

In 2003 we modified this facility to measure the light emission spectrum of scintillation crystals as a function of wavelength and temperature. Figure 1.11 shows the apparatus. A 50 MBq ^{90}Sr electron source irradiates a CsI crystal kept at liquid nitrogen temperature. The monochromator is equipped with a spherical mirror to image the entrance slit with parallel light to the exit slit after the grating. The crystal is located on a cold finger (see fig. 1.11, right) at the focus of the monochromator. To reach liquid nitrogen temperatures a good vacuum is needed to prevent heat flow through the short distance (1 mm) between the cold finger and the wall of the chamber at room temperature. A turbo vacuum pump is used and a vacuum below 2×10^{-6} mbar can be achieved. The Echelette grating is slowly rotated while the light intensity is measured with a photomultiplier. The current of the photomultiplier is integrated and measured with an electrometer.

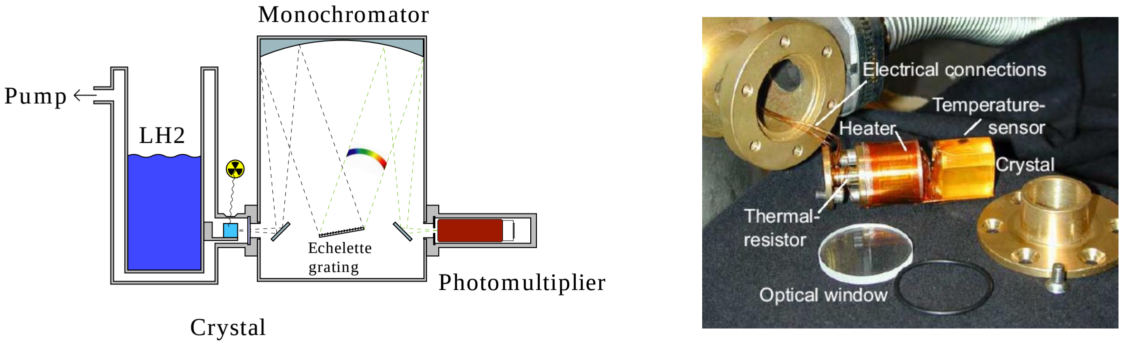

Figure 1.11: *Left: optical spectrometer to measure the light yield of scintillator crystals as a function of temperature and wavelength. Right: cold finger and vacuum chamber. The crystal is attached to the copper support with a capton tape. The brass piece on the right is used to press the optical window to the gasket ring and fits into the entrance slit of the monochromator.*

Data were taken in temperature steps of 10 K between 90 and 230 K for wavelengths between 240 and 450 nm. The emission spectrum contains two lines (fig. 1.12, left) which were fitted with gaussians and a smooth background. The relative intensities of the fitted emission lines at 297 and 332 nm are shown in fig. 1.12 (right) as a function of temperature. The presence of two emission lines in pure cold CsI was already known before [10]. However, our measured intensity distributions are much more precise.

1.5 R&D for laser spectroscopy

In 2003 our group group was involved in the preparation of the spectroscopy phase, namely the construction of a laser system to generate 243 nm light for 1s-2s two-photon spectroscopy in antihydrogen [11]. We used the well known non-linear technique to generate 243 nm light from a laser source of longer wavelength. The laser system consists of a Kr^+ ion laser that emits 4 W in the range 406 nm to 415 nm. The (up to 6 W) Kr^+ ion laser pumps a dye laser which emits in the range 460 nm to 516 nm. The dye laser is tuned to a wavelength of 486 nm which is twice the wavelength of the two-photon 1s-2s transition in (anti)hydrogen. Most of the equipment was provided by the University of Aarhus. A photograph of the two lasers is shown in fig. 1.13 (left).

The light from the dye laser is sent into an external frequency doubling cavity containing a non-linear crystal. The second harmonic generation power in the crystal is maximum when the refractive indices n for the fundamental and the second harmonics are equal. Since the refractive index depends on frequency, a birefringent crystal with a suitably oriented optical axis is used, in which the ordinary ray is chosen for the fundamental frequency and the extraordinary ray for the second harmonic, i.e. $n_o(\omega) = n_e(2\omega)$. Losses are reduced by using a crystal cut such that the light with fundamental

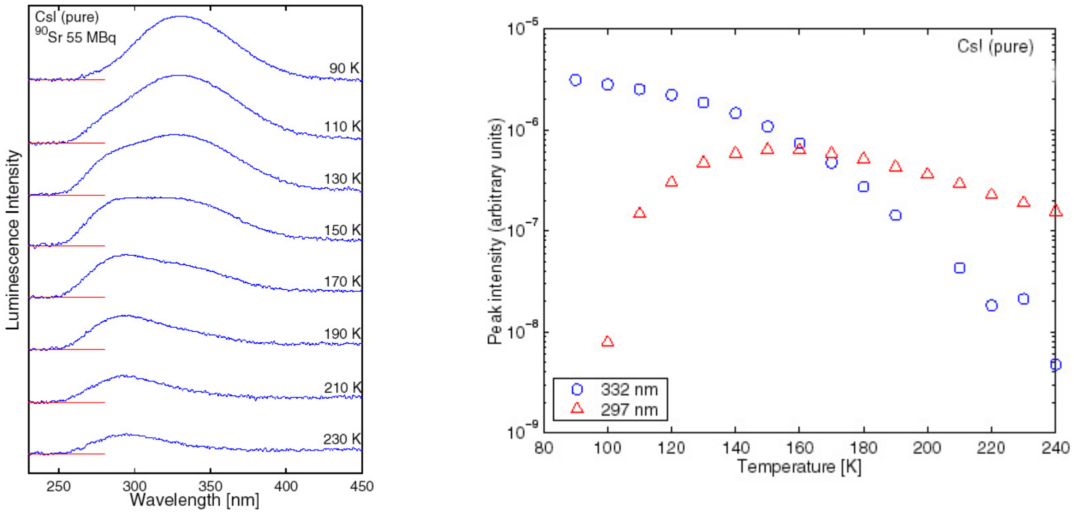

Figure 1.12: *Left: emission spectra from pure CsI crystal at different temperatures. The logarithmic vertical scale is in arbitrary units. Right: intensity of the emission lines at 332 nm and 297 nm as a function of temperature.*

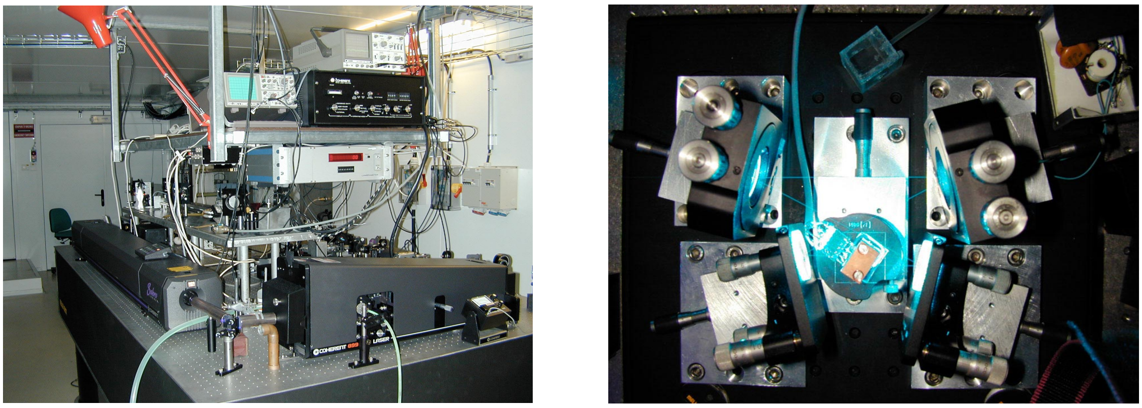

Figure 1.13: *Left: photograph of the krypton and dye lasers on the optical bench. Right: photograph of the lasing cavity. The crystal is mounted inside the temperature stabilized copper block in the center of the picture.*

frequency traversing the crystal penetrates the crystal under the Brewster angle. Under this angle the polarisation parallel to the plane formed by the incident beam and the normal to the crystal surface is not reflected but transmitted into the crystal. The wavelength can be measured accurately with a Michelson interferometer with moving mirrors, calibrated on a He-Ne laser.

The cavity - fig. 1.13 (right) - consists of a Brewster cut rhomb shaped beta barium borate (BBO) crystal of dimensions $5 \times 5 \times 8$ mm^3. The light from the dye laser enters from the right. The convex mirrors have a reflection coefficient of 100 % for the first harmonic and a transmission coefficient of 95 % for the second harmonic. One of the mirrors is mounted on piezoelectric crystal to vary the optical pathlength in the cavity. The beam is sent to a photodiode for cavity locking. The cavity was developed by the Zurich team and the mechanical stability of the piezo was investigated in details [11]. The support structure and temperature stabilized crystal holder (to better than 0.1°) were built in the mechanical workshop of our institute.

Figure 1.14 (left) shows the tuning of 486 nm light from the dye laser. Unfortunately the specified output power of the dye laser (360 mW of power at 486 nm for 3 W input power) could not yet be achieved. The power output is an order of magnitude smaller than expected. However, second harmonic generation of 243 nm UV light was achieved in the BBO cavity. Figure 1.14 (right) shows the output power at 243 nm as a function of input power at 486 nm. The measurement agree with the prediction that the second harmonic power increases with the square of the input power (curve).

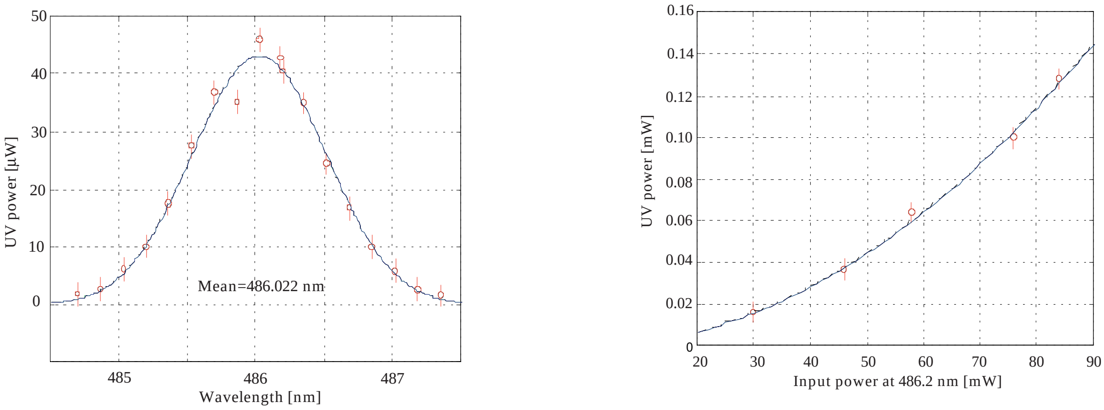

Figure 1.14: *Left: tuning the dye laser to 486 nm (input power 45 mW). Right: 243 nm cavity output power as a function of 486 nm input power. The curve shows the expected quadratic dependence.*

References

[1] M. Amoretti *et al.*, Nature **419** (2002) 456
[2] M. Amoretti *et al.*, Phys. Rev. Lett. **91** (2003) 055001
[3] C. Regenfus, Nucl. Instr. and Meth. in Phys. Res. **A 501** (2003) 65
[4] M. Amoretti *et al.*, Nucl. Instr. and Meth. in Phys. Res. **A 518** (2004) 679
[5] M. Amoretti *et al.*, Phys. Lett. **B 578** (2004) 23
[6] M. Amoretti *et al.*, submitted to Phys. Lett. **B**
[7] M. Amoretti *et al.*, Phys. Lett. **B 583** (2004) 59
[8] C. Amsler *et al.*, Nucl. Instr. and Meth. in Phys. Res. **A 480** (2002) 494
[9] A. Glauser, Diplomarbeit, Universität Zürich, 2003
[10] H. Nishimura *et al.*, Phys. Rev. **B 51** (1995) 2167
[11] O. Iannarelli, Diplomarbeit, Universität Zürich, 2004

2 Particle Physics with CMS at LHC

C. Amsler, V. Chiochia, A. Dorokhov, C. Hörmann, K. Prokofiev, H. Pruys,
C. Regenfus, P. Robmann, T. Speer, and S. Steiner

In collaboration with: ETH-Zürich, Paul Scherrer Institut (PSI), Universität Basel
and the CMS Collaboration.

2.1 Introduction

During 2003 our group continued to design and test the pixel sensors and readout chips for the innermost vertex detector of the CMS experiment. We are also involved in the charged particle reconstruction software and the workshop of our institute is developing the support structure and service tube for the pixel detector.

The CMS (Compact Muon Solenoid) at the Large Hadron Collider (LHC) will start operating at CERN in 2007. Our group will concentrate on physics involving the b- and t-quarks quark, e.g. b-quark production associated with the formation of Higgs bosons. The most interesting events at LHC will contain one or several b-jets originating from the decay of B mesons, with typical mean free paths of a few mm. To allow for efficient tagging of B mesons among the large background of light quark and gluon jets, the detection system has to follow particles towards the primary vertex. The silicon pixel detector we are developing is the closest detector to the interaction point, located only 4 cm from the beam-beam interaction point. The extremely high particle flux near the primary vertex ($\sim$ 1000 particles every 25 ns) requires the innermost tracking layers to be composed of pixel devices delivering 3D coordinates with high resolution and no ambiguity.

The barrel pixel detector consists of three concentric cylindrical layers, 53 cm long with radii of 4.4, 7.3 and 10.2 cm. The layers contain some 3×10^7 silicon pixels. The pixel modules consist of thin, segmented sensor plates with highly integrated readout chips connected by indium bump bonds (fig. 2.1). The final pixel size will be 100×150 μm^2. The analogue signals are read out to determine the coordinates more accurately, using charge sharing between adjacent pixels.

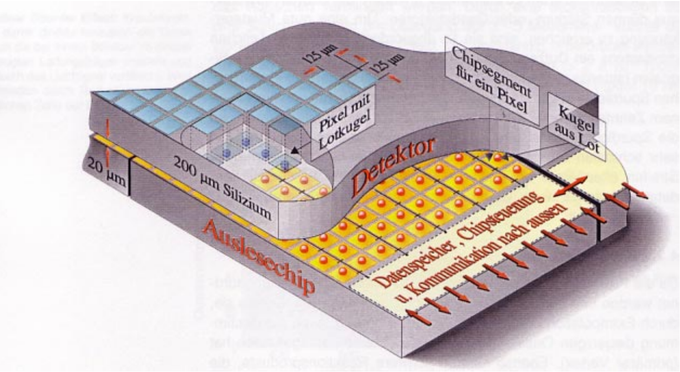

Figure 2.1: *Schematic view of a pixel detector element. Each sensor pixel is connected through an indium solder bump to as pixel unit cell on the readout chip which amplifies and processes the signal. The data are stored on the edge of the chip where they wait for trigger confirmation.*

2.2 Development of pixel sensors

The CMS pixel sensors are manufactured using the "n-on-n" technique consisting of n^+-structures on n-bulk silicon. This allows the partially depleted operation of highly irradiated sensors after type inversion, but also requires inter-pixel isolation. Two isolation techniques were considered for our latest prototypes: p-spray [1], for which a uniform average dose of p-impurities ($\approx 10^{12}$ cm^{-2}) covers the whole structured surface, and p-stop rings ($\approx 10^{13}$ impurities cm^{-2}) which surround the n^+-implants (fig. 2.2). Possible failures of the pixel bump-bonds require a method to evacuate the charge. This is achieved with a bias grid and punch-through structures for the p-spray detectors and by openings in the rings for the p-stop detectors.

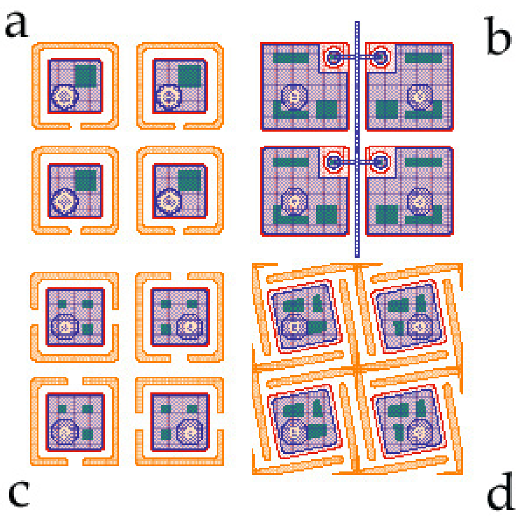

Figure 2.2: *Some of our favorite designs for the pixel sensors. Open p-stop rings (a and c), p-stop crosses (d) and p-spray with bias grid (b).*

Test measurements were performed in the H2 beam line of the CERN SPS in June and September 2003 using 150-225 GeV pions. The test devices contained 22 × 32 pixels with a total sensitive area of 2.75×4 mm^2, and a thickness of 280 μm. The readout pitch was still of the old design, 125 μm × 125 μm. Some of these devices had been previously irradiated in a 24 GeV proton beam at the CERN PS. The sensors received total particle fluences of 3.3×10^{14} $\mathrm{n_{eq}/cm^2}$, 8.1×10^{14} $\mathrm{n_{eq}/cm^2}$ and 1.1×10^{15} $\mathrm{n_{eq}/cm^2}$. They were bump bonded to non-irradiated readout chips of the DMILL type.

The hit coordinates in the pixel detector were determined accurately with our silicon reference telescope [2]. The beam telescope consisted of 4 modules, each with two orthogonal 300μm thick single-sided silicon detectors (32×30 mm^2) with a strip pitch of 25 μm and a readout pitch of 50 μm. The resulting intrinsic resolution of the beam telescope was around σ = 1 μm.

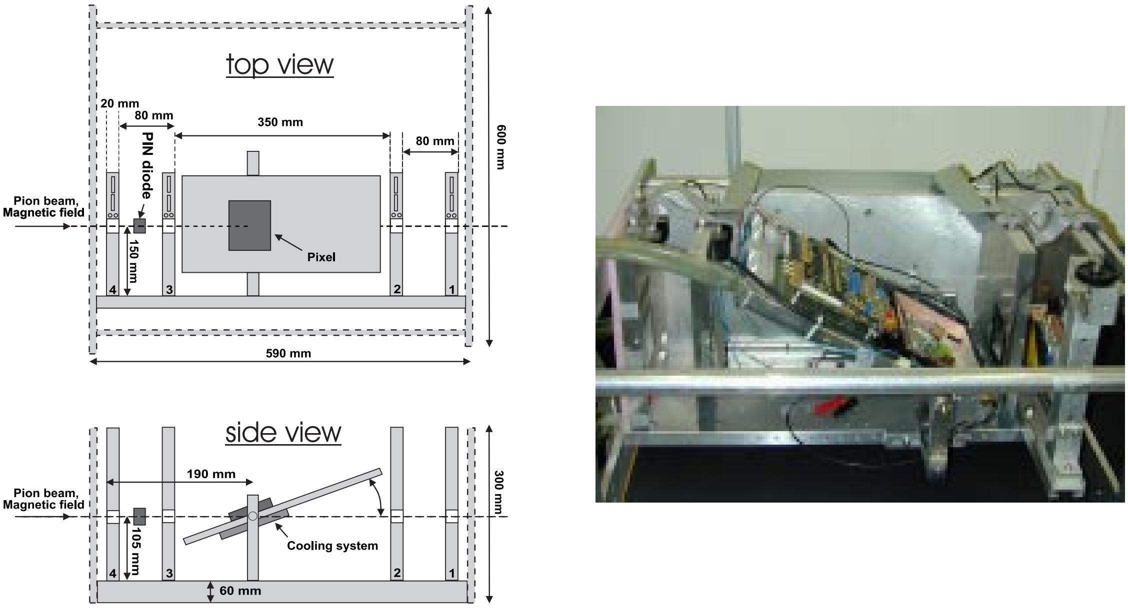

Figure 2.3: *Left: top and side views of the beam telescope. Right: beam telescope setup.*

The pixel sensor with the readout chip was mounted on a rotating support positioned between the second and the third module (fig. 2.3). A trigger signal was generated by a PIN diode. The data acquisition system and slow control (temperature and bias voltag) were written in LabView and LabWindows CVI (National Instruments) running on a PC. The analog signals were digitized in a VME based readout system by FADCs. The setup was located in an open 3 T Helmholtz magnet with magnetic field parallel to the beam. The pixel sensors were cooled with water cooled Peltier elements. Similar measurements were performed earlier by our group [3, 4] but irradiated sensors could not be tested reliably because they were not cooled down to the -10° C foreseen for the CMS tracker. A more detailed discussion of the latest beam test results can be found in ref. [8].

2.2.1 Lorentz angle measurements

The Lorentz angle was obtained by the direct measurement of the charge drift in the magnetic field using the grazing angle method [4]. The pion beam which was in direction of the magnetic field entered the sensor surface at a shallow angle $\alpha = 15^\circ$ (fig. 2.4, left). The deposited charge drifts according to the combined electric and magnetic forces, resulting in a deflection of the particle track projection on the surface by the angle β from which the Lorentz angle Θ_L could be obtained. The deflection observed at 3 T magnetic field is illustrated in fig. 2.4 (right) for the non-irradiated p-spray sensor.

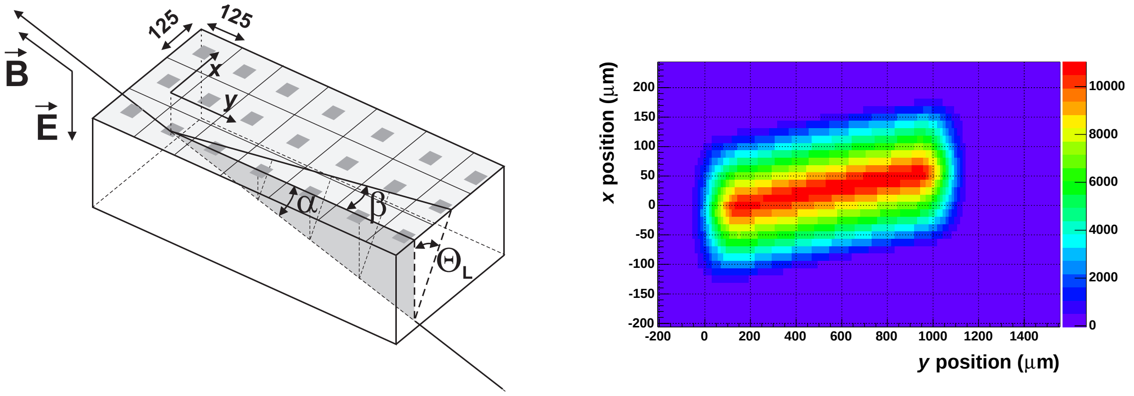

Figure 2.4: *Left: Lorentz angle measurement with the grazing angle method. Right: deflection of the drifting charge in a 3 T magnetic field.*

The angle β was measured by slicing the histogram perpendicularly to the y-axis. The x position of the charge center is shown in fig. 2.5 (left) as a function of y. A measurement without magnetic field is used to correct for detector misalignment with respect to the beam (bottom line). For the irradiated device there are two regions with different slopes, and hence two different Lorentz angles. This behaviour can be explained by the non-linear behaviour of the electric field in the irradiated devices (see next section). Since most of the signal charge is collected from the region close to the pixel implant, this region was used to determine the Lorentz angle.

Figure 2.5 (right) shows the measured Lorentz angles for non-irradiated and irradiated sensors, extrapolated to 4 T. One observes a strong dependence of the Lorentz angle on the bias electric field, which is weakly affected by irradiation and does not depend strongly on sensor design. For the non-irradiated sensors a Lorentz angle of 26° can be reached at a bias voltage of 100 V, while irradiated sensors have to be operated at much higher bias voltages, where the Lorentz angle drops to roughly 10°. Our results are in a good agreement with other measurements and simulations [5].

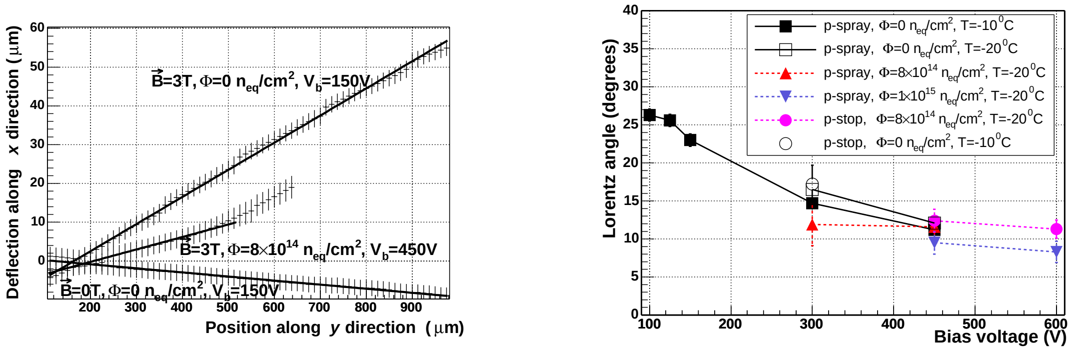

Figure 2.5: *Left: deflection of the collected charge as a function of the y-position. The solid line is the fit. Right: Lorentz angle as a function of bias voltage for a magnetic field extrapolated to 4 T.*

2.2.2 Charge collection in irradiated sensors

Following irradiation, the amount of collected charge decreases due to charge trapping and partial depletion of the sensor. Measurements of the charge collection efficiency as a function of sensor depth were performed using the grazing angle method, this time with magnetic field off. The charge collected in non-irradiated and irradiated p-spray sensors as a function of depth is shown in fig. 2.6 (left). In the non-irradiated sensor the charge is collected uniformly across the whole sensor depth, while the irradiated devices exhibit a different behaviour. At low bias voltages charge is also collected from the side opposite to the pixel implants which could indicate that the depletion starts from both sides of the detector, due to the non-linear behaviour of the electric field. The fraction of collected charge for different designs and irradiation doses is shown in fig. 2.6 (right) as a function of bias voltage.

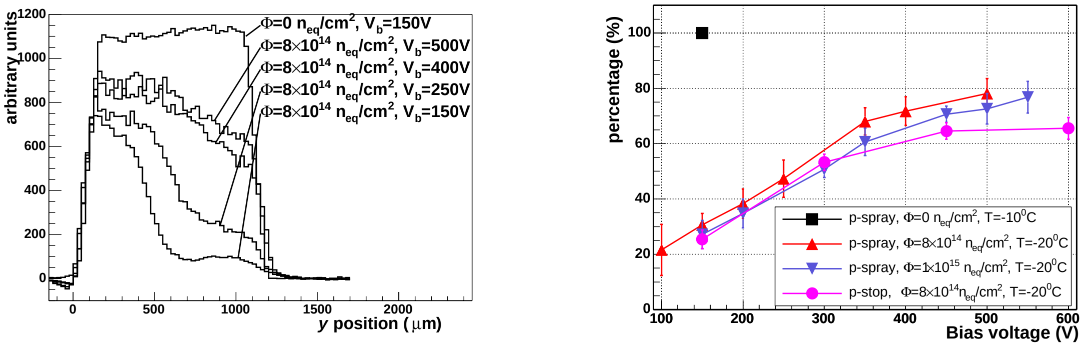

Figure 2.6: *Left: charge collected for different bias voltages. Right: total collected charge normalized to non-irradiated device.*

Charge collection also depends on the position of the incident particle with respect to the pixel implant since the gaps between pixels have a reduced sensitivity. The average charge collected is shown in fig. 2.7 as a function of position for non-irradiated and irradiated sensors. The signal-to-noise ratio decreases from 65 to 35 after irradiation. Thus the CMS pixel detector will operate up to the maximum expected irradiation dose. Note that the area with reduced charge collection between pixels is larger for the p-stop design.

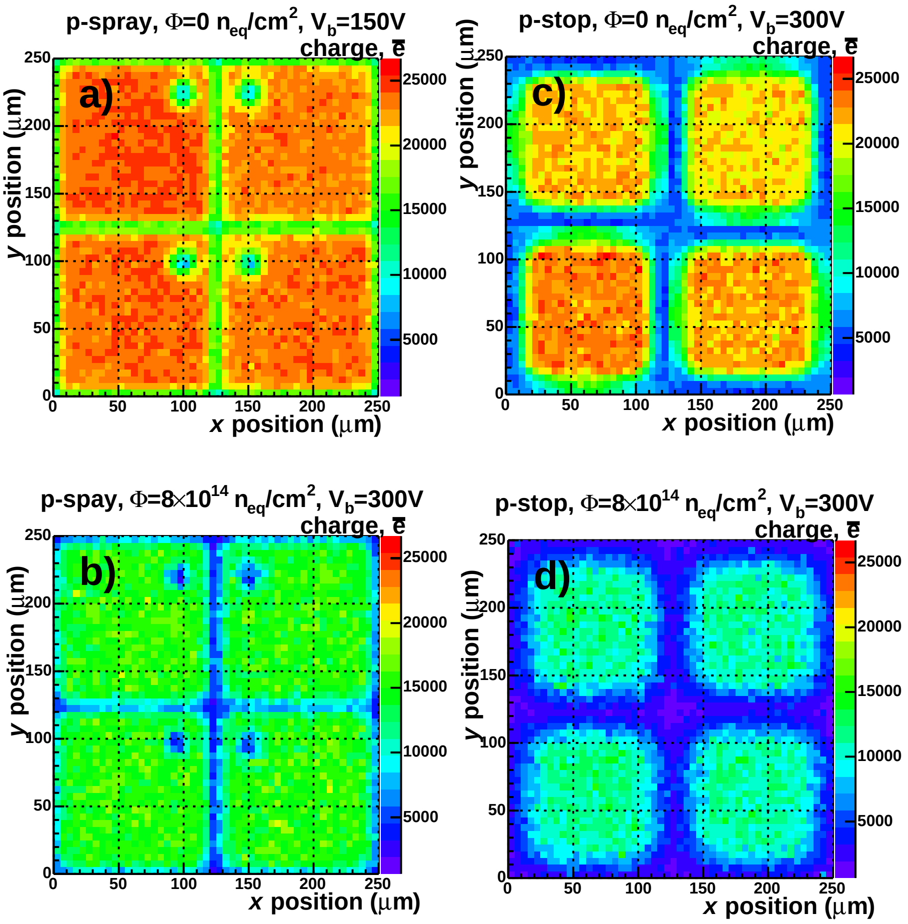

Figure 2.7: Distribution of charge collected in the pixels. The top plots show the non-irradiated p-spray (a) and p-stop designs (c), the bottom plots the respective irradiated sensors.

2.3 Development of the pixel readout chip

We collaborate with PSI in the design of the readout chip (ROC) [6]. The prototype (PSI46) in quarter micron technology DSM (Deep Sub Micron) was submitted and delivered by the manufacturer in 2003. The previous chips had been processed in radiation hard DMILL technology. DSM technology is a well known standard process, significantly cheaper than DMILL which was especially developed for radiation hard devices. However, DSM designs can also be radiation hard. We expect a better yield with DSM than with DMILL and, indeed, the preliminary yield is 80% for DSM, compared with 20% for our previous DMILL chips (PSI43). Power consumption is also lower in DSM which requires only half of the supply voltage and half of the current, hence a quarter of the total power consumption.

DSM technology also offers new possibilities in designing chips and improving their performances. There are five metal layers available for routing instead of only two, and the smallest feature size is 0.25 μm, compared to 0.8 μm for DMILL. Hence more complex circuits can be designed to cope with the updated requirements at LHC: the three layers of pixel detectors will now be operated at high luminosity, including the innermost at 4 cm from the interaction vertex. In DMILL technology, however, we would have an unacceptable fraction of lost data.

The wafer submitted to the manufacturer in 2003 contained four versions of the ROC which differ essentially in the power decoupling scheme (to minimize cross talk and therefore allow lower comparator thresholds) and the total area of metal insulator metal capacitors. Test circuits for internal measurements at points that are not accessible in the ROC were also foreseen in the wafer. In particular, we designed a circuit to investigate single event upsets, see below.

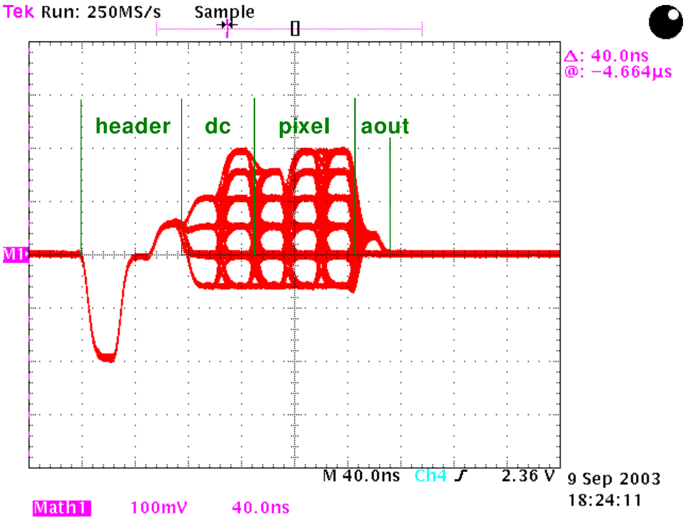

Figure 2.8: *Event readout structure of PSI46 (see text).*

The analog readout of the ROC was tested in the laboratory (fig. 2.8). The first three cycles are used for the header, the next two for the double column address and the following three for the pixel addresses. The addresses are coded by six analog levels which are clearly distinguishable in fig. 2.8. The last cycle is the analog pulse height. The cycles for the address of the double column, the pixel address and the pulse height are repeated for each hit. The readout frequency is 40 MHz.

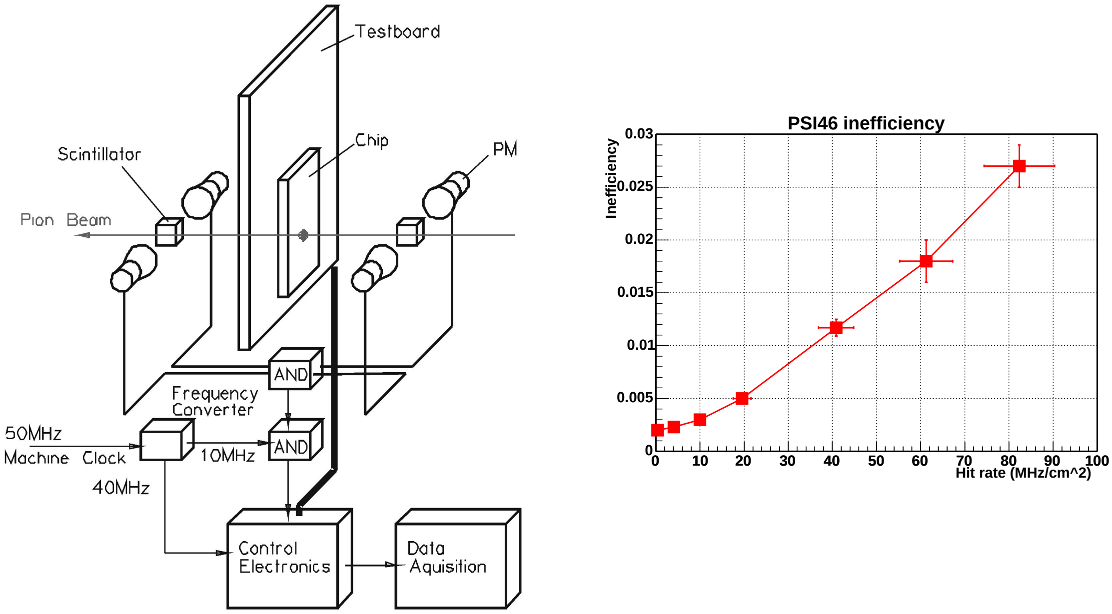

Figure 2.9: *Left: test beam setup. Right: data loss measured with test pions.*

The ROC was tested on the 300 MeV/c πE_1 beamline at PSI. One of the goals was to investigate the data loss under LHC equivalent intensities. The beam intensity varied up to $8{\times}10^7$ pions/cm^2 which corresponds to the expected track density at CMS for the middle layer of the pixel detector. The experimental layout is shown in fig. 2.9 (left). The trigger signal was generated by scintillators and reduced to 10 kHz by coincidence with the random signal of a radioactive source. The ROC was operated with a synchronized 40 MHz frequency which corresponds to the bunch crossing frequency at LHC.

The inefficiency versus fluence is shown in fig. 2.9 (right). The data loss of PSI46 (2.5 % at the maximum luminosity) is about an order of magnitude smaller than that of PSI43, but still somewhat higher than expected. Hence the translation of the ROC from DMILL to DSM was successful and the new chip is much more performant. Some minor improvements are, however, still necessary.

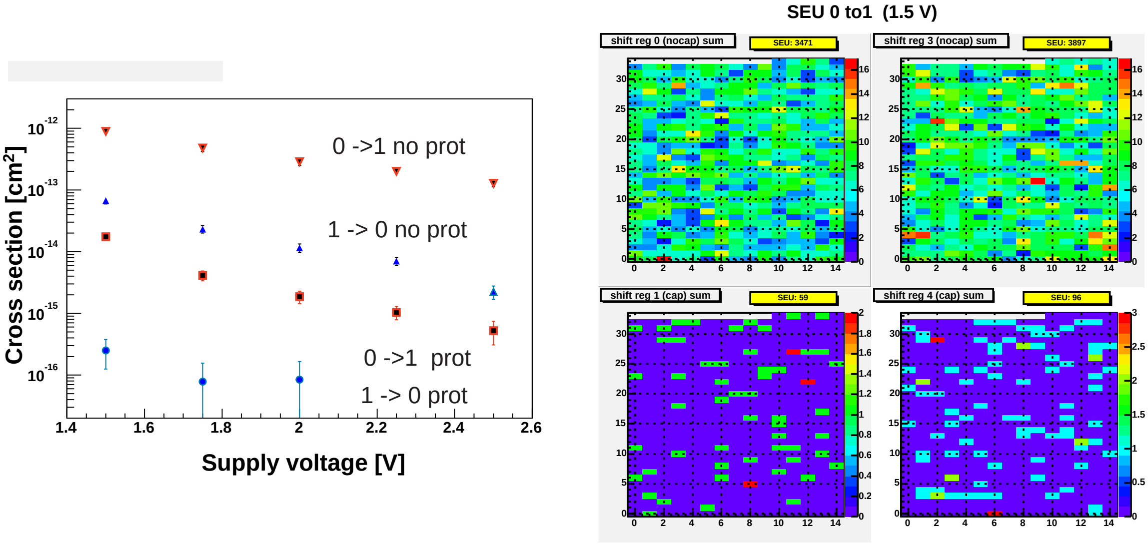

Figure 2.10: *Left: SEU cross sections for 300 MeV/c π^+ on the SEU test structures for various supply voltages. Right: accumulated spatial distribution of SEUs after 160 readouts for four shift registers in parallel. The upper row shows the distribution of two unprotected shift registers and the lower one the distribution for two protected shift registers.*

Single event upsets (SEU) occur during high energy deposits in a small sensitive volume of the electronics circuit, leading to unwanted bit flips. SEU events are due to hadronic interactions with nuclei on the lattice. This is a known problem, e.g. in space applications, which has also to be taken seriously at LHC. SEU is more dangerous in DSM technology due to smaller node capacities, faster circuits and lower supply voltages, and is a serious problem for detector control functions. For example, the analog converter values and trimbits for the thresholds are stored in memory cells. In order to deal with the SEUs, one has to reload permanently the storage cells, which causes unnecessary data traffic.

In our measurements we investigated the effects of capacitors as protections against SEUs. The SEU test structures designed in DSM technology consisted of shift registers protected by capacitors. The shift registers were filled with 1 or 0 and read out every 5 minutes to count the flipped bits. The cross sections for bit flips are shown in figure 2.10 (left) as a function of supply voltage. The cross sections for SEU are roughly two orders of magnitude smaller with protective capacitor.

Another interesting result is the asymmetry in the probabilities for 1 to 0 flips and 0 to 1 flips. The ratio of probabilities $0 \rightarrow 1 / 1 \rightarrow 0$ is about 120. Figure 2.10 (right) shows the spatial distribution of SEUs after 160 readouts of 5 minutes each, at a supply voltage of 1.5 V. The upper row shows the spatial distribution of SEUs in the unprotected shift registers and the lower row shows the distribution for the protected cells.

By histogramming the number of SEUs after each readout one obtains a Poisson distribution. This is a hint for independent single pixel upsets and no clusterisation of SEUs. The ratio of SEU cross sections for π^+/π^- is 1.6. The ratio for π^+/p ($\sim$ 5) was also measured using 500 MeV/c protons.

This is an important measurement since most investigations for space applications were done with protons.

2.4 Event reconstruction software

We are developing techniques to reconstruct the interaction vertex in CMS within the object-oriented reconstruction framework (ORCA). After having implemented in ORCA a single-vertex fit algorithm using the Kalman filter formalism (see last year's annual report and ref. [7]), we are now developing an algorithm based on a the so-called Gaussian sum filter.

The usual vertex reconstruction algorithm is the Kalman filter based on a least square minimization, which hence assumes that the track measuring errors follow a normal distribution. However, a non-Gaussian noise (due e.g. to δ-electrons) is always present. One method that takes non-Gaussian effects into account is the Gaussian-sum filter (GSF) in which the measurement errors are modelled by a superposition of several (mostly two) Gaussians which we shall refer to as *components*. It is a non-linear estimator, in which the weights of the components depend on the measurements.

In an iterative procedure, the estimate of the vertex is updated with one track at the time. The vertex consists of several solutions calculated with all possible components of the tracks. When one track is added to the vertex, each solution for the vertex is combined with each component of the new track, using the Kalman filter. The final vertex estimate is then calculated as the weighted average of all solutions. Since the number of solutions increases exponentially, it has to be limited to an acceptable number. This is achieved by merging solutions which are close enough.

To investigate the performance of a such an algorithm we made a simulation using vertices leading to four-tracks. No track reconstruction was performed but track parameters were smeared according to a two-component Gaussian model. The component modelling the non-Gaussian tails had a standard deviation ten times larger than that of the core component and their relative weights were 9:1.

For a fit with the Kalman filter, for which only one component is used, the distributions of the vertex pulls (difference between simulated and reconstructed values divided by the measurement error) show a Gaussian core with tails (fig. 2.11a) and a large fraction of the fitted events have a very small χ^2-probability (fig. 2.11b).

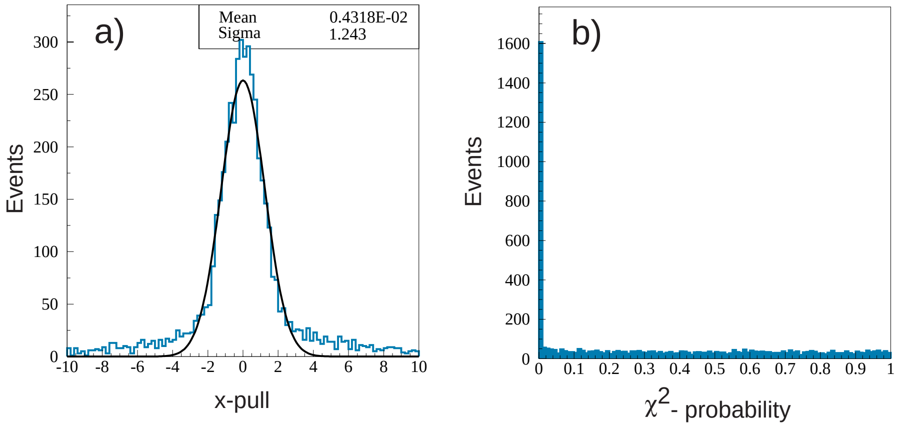

Figure 2.11: *a) Pull of the reconstructed vertex x-coordinate; b) χ^2-probability distribution for the Kalman filter.*

In the GSF method the two components are used, each with the correct weight and variance. The pulls have a resolution closer to unity when fitted with a Gaussian, the tails vanish (fig. 2.12a) and the peak at low χ^2 disappears (fig. 2.12b). This indicates that the error estimates and component weights were reasonable. These encouraging tests demonstrate the power of the algorithm and its efficiency in the presence of non-Gaussian noise.

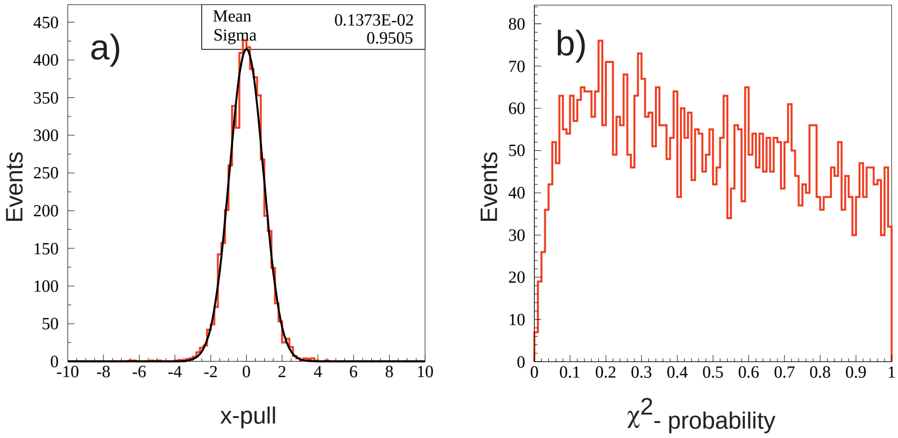

Figure 2.12: *a) Pull of the reconstructed vertex x-coordinate; b) χ^2-probability distribution for the GSF (see text).*

We are also developing a kinematic fit using the Lagrange multiplier method which incorporates additional constraints into the vertex fit. Additional constraints such as masses of decaying particles, energy and momentum conservation, will improve the resolution. A further constraint of interest would require the momentum of the reconstructed B meson to be parallel to the vector pointing from the primary to the secondary vertex (pointing constraint).

As an example, consider the decay $B_s \to J/\psi\, \phi \to K^+K^-\mu^+\mu^-$. The invariant mass of the four tracks after the vertex fit but without any additional constraint is shown in fig. 2.13a. The distribution has a Gaussian width of about 40 MeV and the average mass is displaced by some 13 MeV compared to the table value. This is due to the large error on the muon momentum measurement in the CMS detector.

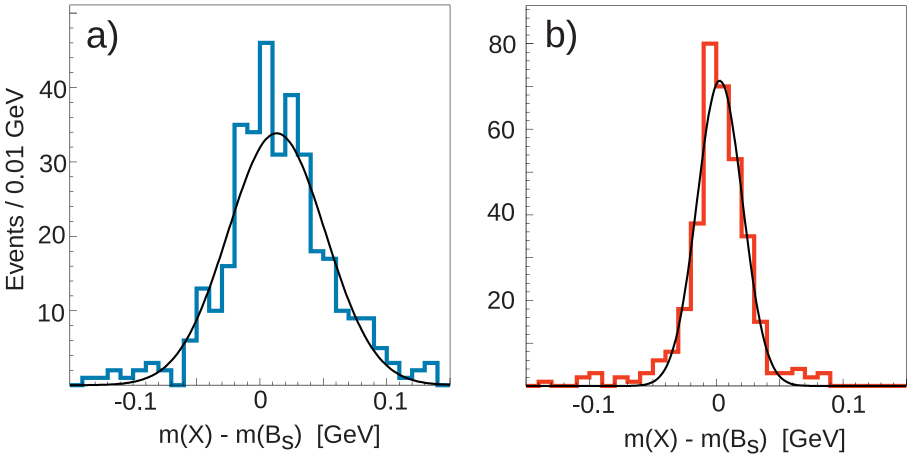

Figure 2.13: $K^+K^-\mu^+\mu^-$ *invariant mass in* $B_s \to J/\psi\, \phi \to K^+K^-\mu^+\mu^-$ *before (a) and after the* J/ψ *mass constraint (b).*

However, the invariant mass distribution becomes significantly narrower and correctly centered when the four-momentum of the two-muon system is constrained to match the J/ψ mass (fig. 2.13b).

This constraint is applicable due to the very small width of the J/ψ compared to the measurement uncertainties of typically 10 MeV.

References

[1] R. H. Richter *et al.*, Nucl. Instr. and Meth. in Phys. Res. **A 377** (1996) 412

[2] C. Amsler *et al.*, Nucl. Instr. and Meth. in Phys. Res. **A 480** (2002) 501

[3] R. Kaufmann, PhD Thesis, Universität Zürich, 2001

[4] B. Henrich and R. Kaufmann, Nucl. Instr. and Meth. in Phys. Res. **A 477** (2002) 304

[5] V. Bartsch *et al.*, Nucl. Instr. and Meth. in Phys. Res. **A 478** (2002) 330
V. Bartsch *et al.*, Nucl. Instr. and Meth. in Phys. Res. **A 497** (2003) 389

[6] M. Barbero *et al.*, Nucl. Instr. and Meth. in Phys. Res. (in print)

[7] R. Frühwirth, K. Prokofiev, T. Speer, P. Vanlaer and W. Waltenberger, Nucl. Instr. and Meth. in Phys. Res. **A 502** (2003) 699

[8] A. Dorokhov *et al.*, to appear in Nucl. Instr. Meth. in Phys. Res. **A** preprint physics / 0311050;
T. Rohe *et al.*, submitted to IEEE-TNS 7, preprint physics / 0312009

3 Publications

Articles

- Positron plasma diagnostics and temperature control for antihydrogen production
  M. Amoretti et al. (ATHENA Collaboration)
  Phys. Rev. Lett. 91 (2003) 055001

- Detection of antihydrogen annihilations with a cryogenic pure-CsI crystal detector
  C. Regenfus, C. Amsler, A. Glauser, D. Grögler, D. Lindelöf, H. Pruys
  Nucl. Instr. Meth. in Phys. Res. A 504 (2003) 343

- Limits on the neutrino magnetic moment from the MUNU experiment
  Z. Daraktchieva et al. (MUNU Collaboration)
  Phys. Lett. B 564 (2003) 190

- A measurement of the neutrino magnetic moment at the Bugey nuclear reactor
  O. Link
  Inaugural Dissertation, Universität Zürich, 2003

- The ATHENA antihydrogen apparatus
  M. Amoretti et al. (ATHENA Collaboration)
  Nucl. Instr. and Meth. in Phys. Res. A 518 (2004) 679

- Annihilation at rest of antiprotons and protons into neutral particles
  C. Amsler et al. (CRYSTAL BARREL Collaboration)
  Nucl. Phys. A 720 (2003) 357

- Production and decay of $\eta'(958)$ and $\eta(1440)$ in $\bar{p}p$ annihilation at rest
  C. Amsler et al. (CRYSTAL BARREL Collaboration)
  Eur. Phys. J. C 33 (2004) 23

- Mesons beyond the naive quark model
  C. Amsler and N. A. Törnqvist
  Physics Reports 389 (2004) 61

- High rate production of antihydrogen
  M. Amoretti et al. (ATHENA Collaboration)
  Phys. Lett. B 578 (2004) 23

- Antihydrogen production temperature dependence
  M. Amoretti et al. (ATHENA Collaboration)
  Phys. Lett. B 583 (2004) 59

- A cryogenic silicon microstrip and pure-CsI detector for detection of antihydrogen annihilations
  C. Regenfus
  Nucl. Instr. and Meth. in Phys. Res. A 501 (2003) 65

- A. Glauser
  Development of APD readout for pure-CsI crystals at cryogenic temperatures
  Nucl. Instr. and Meth. in Phys. Res. A 504 (2003) 347

- A. Dorokhov, A. Glauser, Y. Musienk, C. Regenfus, S. Reucroft and J. Swain
  Study of the Hamamatsu avalanche photodiode at liquid nitrogen temperatures
  Nucl. Instr. and Meth. in Phys. Res. A 504 (2003) 58

- New Developments in Vertex Reconstruction for CMS
  R. Frühwirth, K. Prokofiev, T. Speer, P. Vanlaer and W. Waltenberger
  Nucl. Instr. and Meth. in Phys. Res. A 502 (2003) 699

- Vertex reconstruction framework and its implementation for CMS
  T. Boccali, R. Frühwirth, W. Waltenberger, K. Prokofiev, T. Speer,P. Vanlaer
  Proc. Conf. on Computing in High Energy and Nuclear Physics, La Jolla (2003)

- New vertex reconstruction algorithms for CMS
  R. Frühwirth, W. Waltenberger, K. Prokofiev, T. Speer, P. Vanlaer, E. Chabanat, N. Estre
  Proc. Conf. on Computing in High Energy and Nuclear Physics, La Jolla (2003)

- The Atlas and CMS trackers
  Thomas Speer
  Proc. 5th Int. Conf. on Hyperons, Charm and Beauty Hadrons, Vancouver (2002), Nucl. Phys. (Proc. Suppl.) 115 (2003) 318

- First production and detection of cold antihydrogen atoms
  M.C. Fujiwara et al. (ATHENA Collaboration)
  Proc. Int. Conf. on Low Energy Antiproton Physics (LEAP'03), Yokohama, Japan
  Nucl. Instr. Meth. in Phys. Res. B 214 (2004) 11

- Temperature dependence of antihydrogen production in the ATHENA experiment
  G. Bonomi et al. (ATHENA Collaboration)
  Proc. Int. Conf. on Low Energy Antiproton Physics (LEAP'03), Yokohama, Japan
  Nucl. Instr. Meth. in Phys. Res. B 214 (2004) 17

Articles in press

- Tests of silicon sensors for the CMS pixel detector
  A. Dorokhov et al.
  Nucl. Instr. and Meth. in Phys. Res. A, preprint physics/0311050

- Position Dependence of Charge Collection in Prototype Sensors for the CMS Pixel Detector
  T. Rohe et al.
  IEEE-TNS 7, preprint physics/0312009

- Detection of antihydrogen annihilations with a Si-microstrip and pure CsI detector
  I. Johnson et al. (ATHENA Collaboration)
  World Scientific

- Design and Test of the CMS Pixel Readout Chip
  M. Barbero et al.
  Nucl. Instr. and Meth. in Phys. Res.

- Study of antiproton annihilation on neutrons into $\omega\pi^-\pi^0$
  C. Amsler et al. (CRYSTAL BARREL Collaboration)
  Phys. Lett. B

- Review of Particle Physics
  S. Eidelman et al. (Particle Data Group)
  Phys. Lett. B

- Light exotic mesons
  C. Amsler
  Proc. Quark Confinement and the Hadron Spectrum V, Gargnano, 2002
  World Scientific

- Vertex reconstruction in CMS
  E. Chabanat et al.
  Proc. vertex 2003, Low Wood, Cumbria, UK, 2003
  Nucl. Instr. and Meth. in Phys. Res.

- A Gaussian sum filter for vertex reconstruction
  T. Speer
  IX Int. Workshop on Advanced Computing and Analysis Techniques in Physics Research, ACAT03, Tsukuba, Japan, 2003
  Nucl. Instr. and Meth. in Phys. Res.

Invited Lectures

- C. Amsler
  Invited talk, Physikalische Gesellschaft Zürich, 19.06.03
  “Glueballe”

- C. Amsler
  Colloquium, Budker Institute of Nuclear Physics, Novosibirsk, 12.9.03
  “Experimental evidence for a large content of glue in the f_0(1500) meson”

- C. Amsler
  Colloquium, Budker Institute of Nuclear Physics, Novosibirsk, 19.9.03
  “Antihydrogen”

- C. Amsler
  Seminar, Laboratory of Theoretical Physics of Sobolev Institute for Mathematics, 24.9.03
  “Exotic mesons”

- C. Amsler
  Colloque, Université de Neuchâtel, 10.11.03
  “Antihydrogen”

- C. Amsler Conférence d’orientation, EPF-Lausanne, 28.1.04
  “Fabrication d’antimatière au CERN”

- V. Chiochia
  Invited talk, 3rd Workshop on radiation hard semiconductor devices for very high luminosity colliders, CERN, 4.11.03
  “Tests of silicon sensors for the CMS Pixel Detector”

- I. Johnson
  Invited talk, 8th ICATPP Conference on Astroparticle, Particle, Space Physics, Detectors and Medical Physics Applications, Como, Italy, 9.10.03
  “Detection of antihydrogen annihilations with a Si-micro-strip and pure CsI crystal detector”

- A. Dorokhov
  Invited talk, 6th International Conference on Large Scale Applications and Radiation Hardness of

Semiconductor Detectors, Florence, Italy 30.11.03
"Tests of silicon sensors for the CMS pixel detector"

- C. Regenfus
  Colloque, Université de Fribourg, 21.5.03
  "Cold Antihydrogen for probing world antiworld symmetry"

- V. Chiochia
  Seminar, DESY, 5.12.03
  "The CMS Pixel Detector: Overview and Test Beam results"

- T. Speer
  Invited talk, IX Int. Workshop on Advanced Computing and Analysis Techniques in Physics Research, ACAT03, Tsukuba, Japan, 4.12.03
  "A Gaussian sum filter for vertex reconstruction"

ATHENA Collaboration (2003):
M. Amoretti, C. Amsler, G. Bonomi, A. Bouchta, P. Bowe, C. Carraro, C. L. Cesar, M. Charlton, M. Doser, V. Filippini, A. Fontana, M. C. Fujiwara, R. Funakoshi, P. Genova, J. S. Hangst, R. S. Hayano, L. V. Joergensen, I. Johnson, V. Lagomarsino, R. Landua, E. Lodi Rizzini, M. Macri, N. Madsen, P. Montagna, H. Pruys, C. Regenfus, P. Riedler, J. Rochet, A. Rotondi, G. Rouleau, G. Testera, A. Variola, D. P. van der Werf

MUNU Collaboration (2003):
C. Amsler, M. Avenier, C. Broggini, J. Busto, C. Cerna, Z. Daraktchieva, G. Gervasio, P. Jeanneret, G. Jonkmans, D.H. Koang, J. Lamblin, D. Lebrun, O. Link, F. Ould-Saada, G. Puglierin, A. Stutz, A. Tadsen, J.-L. Vuilleumier

CRYSTAL BARREL Collaboration (2003):
C. Amsler, C. A. Baker, B. M. Barnett, C. J. Batty, P. Blüm, K. Braune, V. Credé, K. M. Crowe, M. Doser, W. Dünnweber, D. Engelhardt, M. A. Faessler, R. P. Haddock, F. H. Heinsius, N. P. Hessey, D. Jamnik, H. Kalinowsky, P. Kammel, J. Kisiel, E. Klempt, H. Koch, M. Kunze, U. Kurilla, R. Landua, H. Matthäy, C. A. Meyer, F. Meyer-Wildhagen, R. Ouared, K. Peters, B. Pick, M. Ratajczak, C. Regenfus, J. Reinnarth, A. Sarantsev, U. Strohbusch, M. Suffert, J. S. Suh, U. Thoma, S. Wallis-Plachner, D. Walther, U. Wiedner

PARTICLE DATA Group (2003):
K. Hagiwara, K. Hikasa, K. Nakamura, M. Tanabashi, M. Aguilar-Benitez, C. Amsler, R.M. Barnett, P.R. Burchat, C.D. Carone, C. Caso, G. Conforto, O. Dahl, M. Doser, S. Eidelman, J.L. Feng, L. Gibbons, M. Goodman, C. Grab, D.E. Groom, A. Gurtu, K.G. Hayes, J.J. Hernandez-Rey, K. Honscheid, C. Kolda, M.L. Mangano, D.M. Manley, A.V. Manohar, J. March-Russell, A. Masoni, R. Miquel, K. Mönig, H. Murayama, S. Navas, K.A. Olive, L. Pape, C. Patrignani, A. Piepke, M. Roos, J. Terning, N.A. Törnqvist, T.G. Trippe, P. Vogel, C.G. Wohl, R.L. Workman, W.-M. Yao